

Characterization of Direct-Drive-Implosion Core Conditions on OMEGA with Time-Resolved Ar *K*-Shell Spectroscopy

Introduction

In the direct-drive approach to inertial confinement fusion (ICF), capsules are directly irradiated by a large number of symmetrically arranged laser beams.^{1,2} Time-resolved Ar *K*-shell spectroscopy has been established as a reliable technique to diagnose the compressed core of direct-drive implosions,^{3–10} as well as indirect-drive implosions.^{6,11–16} This technique has been used on the 60-beam OMEGA laser system¹⁷ to characterize the core conditions of direct-drive implosions. Plastic shells with an Ar-doped deuterium fill gas were driven with a 23-kJ, 1-ns square laser pulse smoothed with phase plates,¹⁸ 1-THz smoothing by spectral dispersion (SSD),^{19–21} and polarization smoothing (PS) using birefringent wedges.²² Laser beam smoothing reduces the effects of the ablative Rayleigh–Taylor hydrodynamic instability by reducing the initial imprint levels.²³ The targets in this experiment are predicted to have a convergence ratio of ~ 15 . Measured convergence ratios of 14 have been reported for similar capsules on OMEGA.²⁴ The emissivity-averaged core electron temperature and density were inferred from the measured time-dependent Ar *K*-shell spectral line shapes.

Two properties of the Ar *K*-shell spectrum emitted from hot, dense plasmas ($n_e > 10^{23} \text{ cm}^{-3}$; $T_e > 1 \text{ keV}$) are exploited to infer a unique combination of emissivity-averaged core electron temperature and density: (1) The line shapes depend strongly on density and are relatively insensitive to variations in electron temperature. (2) The relative intensities of the Ar *K*-shell lines and their associated *L*-shell satellites are sensitive to variations in electron temperature and density.⁸ The Stark-broadened line profiles for the Ar He β ($1s3l-1s^2$), He γ ($1s4l-1s^2$), He δ ($1s5l-1s^2$), and Ly β ($3l-1s$) resonant transitions and associated satellites were calculated using a second-order quantum mechanical relaxation theory.⁸ These line profiles were combined using relative intensities derived from a detailed non-LTE kinetics code corrected for the effects of radiative transfer using an escape-factor approximation. The Stark-broadened line profiles were corrected for the effects of opacity using a slab opacity model.

In this article we present time-resolved Ar *K*-shell spectroscopic measurements of a direct-drive implosion on OMEGA. The following sections (1) describe experimental setup, including the photometric calibration of the spectroscopic diagnostics; (2) describe the atomic physics model and the line-fitting procedure; (3) compare the modeled spectra with the measured data; and (4) give the inferred temporal evolution of the electron temperature and density. Conclusions are presented in the last section.

Experimental Setup

The layout of the experimental setup on OMEGA and a schematic of the target are shown in Fig. 86.1. The 20- μm -thick, 954- μm -diam plastic shell with an Ar-doped deuterium fill gas was driven with a 24-kJ, 1-ns square laser pulse, and the Ar *K*-shell emission was recorded with time-resolved and time-integrated flat crystal spectrometers. The total fill pressure was 15 atm with an atomic Ar percentage of 0.18 resulting in a partial pressure of Ar of $\sim 0.05 \text{ atm}$. The impact of the Ar dopant on the capsule performance reduces the primary neu-

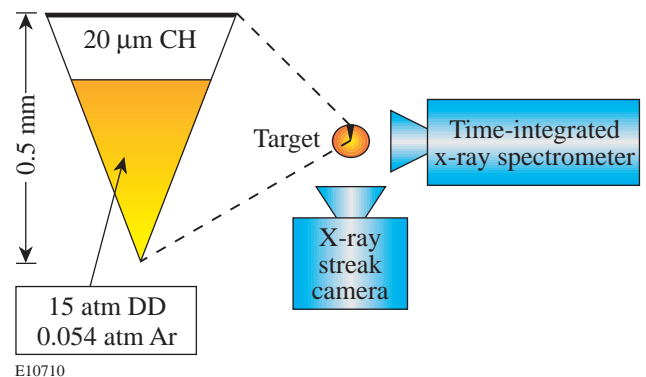


Figure 86.1

The layout of the experimental setup on OMEGA and a schematic of the target. The plastic shell with an Ar-doped deuterium fill gas was driven with a 23-kJ, 1-ns square laser pulse. The total fill pressure was 15 atm with an atomic Ar percentage of 0.18 resulting in a partial pressure of Ar of $\sim 0.05 \text{ atm}$. Streaked and high-resolution, time-integrated x-ray spectra of Ar *K*-shell emission were recorded with flat crystal spectrometers.

tron yield to $\sim 75\%$ of an undoped target.²⁴ The on-target beam uniformity has been significantly improved on OMEGA: single-beam irradiation nonuniformity has been reduced with 1-THz SSD and PS, and the beam-to-beam rms power imbalance is 5% or less for square laser pulses.²⁴

The time-dependent Ar *K*-shell spectral line shapes were monitored using time-resolved x-ray spectroscopy. Two x-ray streak cameras were fielded for this experiment: one had an ~ 2 -ns temporal window and was used to measure the spectral line shapes with 25-ps temporal resolution; the other had an ~ 4 -ns temporal window and was used to measure the absolute timing of the Ar *K*-shell emission with an accuracy of 50 ps.

The spectrum recorded with the faster streak camera is shown in Fig. 86.2 with temporal streak distortions removed. This spectral range includes the following Ar *K*-shell resonance lines: Ar Ly $_{\alpha}$ ($2l-1s$), He $_{\beta}$ ($1s3l-1s^2$), He $_{\gamma}$ ($1s4l-1s^2$), Ly $_{\beta}$ ($3l-1s$), He $_{\delta}$ ($1s5l-1s^2$), He $_{\epsilon}$ ($1s6l-1s^2$), Ly $_{\gamma}$ ($4l-1s$), Ly $_{\delta}$ ($5l-1s$), and Ly $_{\epsilon}$ ($6l-1s$). The prominent ones have been identified in Fig. 86.2. The x-ray streak camera,²⁵ which utilized a flat RbAP (rubidium acid phthalate) crystal to disperse the spectrum onto an Au photocathode, was timed (see Fig. 86.2) to capture the coronal plasma emission at the end of the laser pulse just after 1 ns through the peak x-ray emission at 2 ns. The slower streak camera recorded the same spectral range with a similar spectrometer; however, as shown in Fig. 86.3, it was timed to record the entire evolution of the x-ray emission from the start of the coronal plasma emission when the laser strikes the target to the peak x-ray production at

peak compression. Temporal streak distortions have also been removed from the time-resolved spectra in Fig. 86.3. The time axis of the slower streak camera was established with the temporally modulated ultraviolet fiducial laser pulse (see Fig. 86.3). The exponential rise of the coronal plasma emission was extrapolated back to the beginning of the laser pulse.

The absolute timing of the peak x-ray emission in Fig. 86.2 was taken from Fig. 86.3. The average sweep speed of the faster streak camera was measured to be 48 ps/mm on a subsequent shot during the experimental campaign using a temporally modulated ultraviolet fiducial laser pulse. As seen in Fig. 86.2, the onset of the Ar *K*-shell line emission occurs during the shock heating beginning at ~ 1.6 ns, and as the implosion proceeds, the amount of Stark-broadening increases. The dispersion of the streaked spectrum was determined using the relatively narrow spectral features observed just after the onset of the Ar *K*-shell emission lines at $t = 1.77$ ns (see Fig. 86.4). The modeled spectrum also shown in Fig. 86.4 is discussed in the next section. A portion of the streak camera's x-ray photocathode was blocked, providing a wavelength fiducial (see Fig. 86.2) to establish the orientation of the streak axis. The spectra were recorded on Kodak T-max 3200 film. The film was digitized using a PDS (Perkin-Elmer Photometric Data Systems) microdensitometer and corrected for film sensitivity.

The streaked spectra were corrected for variations in x-ray spectral sensitivity and streak camera flat-fielding effects using the photometrically calibrated spectra of a time-integrated

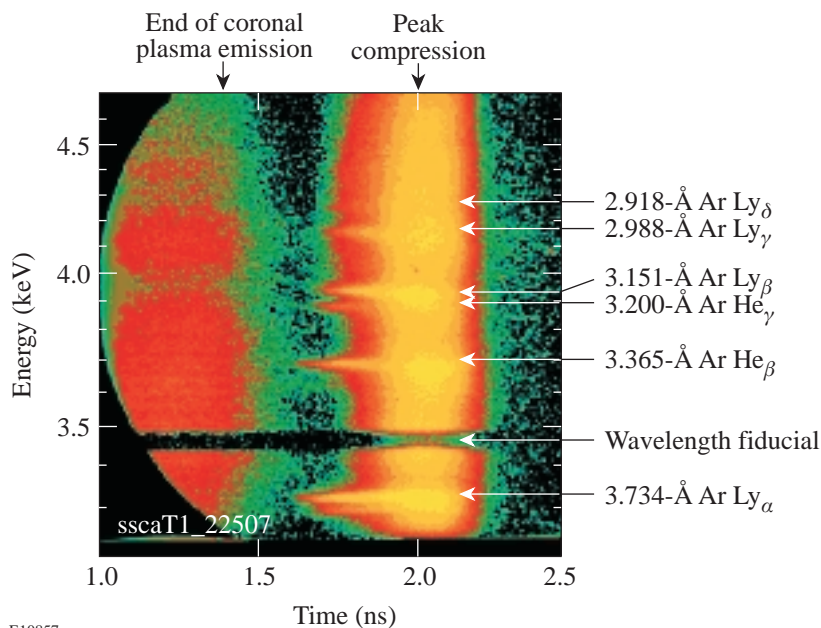


Figure 86.2

The time-resolved Ar *K*-shell spectral measurement with an ~ 2 -ns temporal window for shot number 22507. Temporal streak distortions have been removed, and the orientation of the streak axis is determined with the wavelength fiducial. The onset of the Ar *K*-shell line emission occurs during the shock heating beginning at ~ 1.6 ns, and the Stark-broadening increases as the implosion proceeds. The dispersion of the streaked spectrum was determined using the relatively narrow spectral features observed just after the onset of the Ar *K*-shell emission lines.

spectrometer. The time-integrated instrument utilized an ADP (ammonium dihydrogen phosphate) crystal to disperse the spectrum onto Kodak DEF (direct exposure) film. This instrument was calibrated using a combination of measured and published crystal reflectivities,²⁶ and the film was digitized with the PDS microdensitometer and corrected for film sensitivity. The bremsstrahlung emission from an undoped capsule, which was measured with the time-integrated spectrometer and found to be characteristic of an electron temperature equal to 0.68 keV, was used to calibrate the time-resolved spectra. The streaked spectrum was integrated in time and compared

with the bremsstrahlung emission. The ratio of these two quantities is the photometric calibration of the streaked spectrum. The calibration, which is applied to each time-resolved spectra, is shown in Fig. 86.5.

Atomic Physics Modeling

Time-resolved Ar *K*-shell spectroscopy is a technique that allows the emissivity-averaged electron temperature and density to be inferred. The Stark-broadened Ar *K*-shell spectral line shapes are calculated with the Multi-Electron Radiator Lineshape (MERL) code²⁷ in the manner described in Ref. 8.

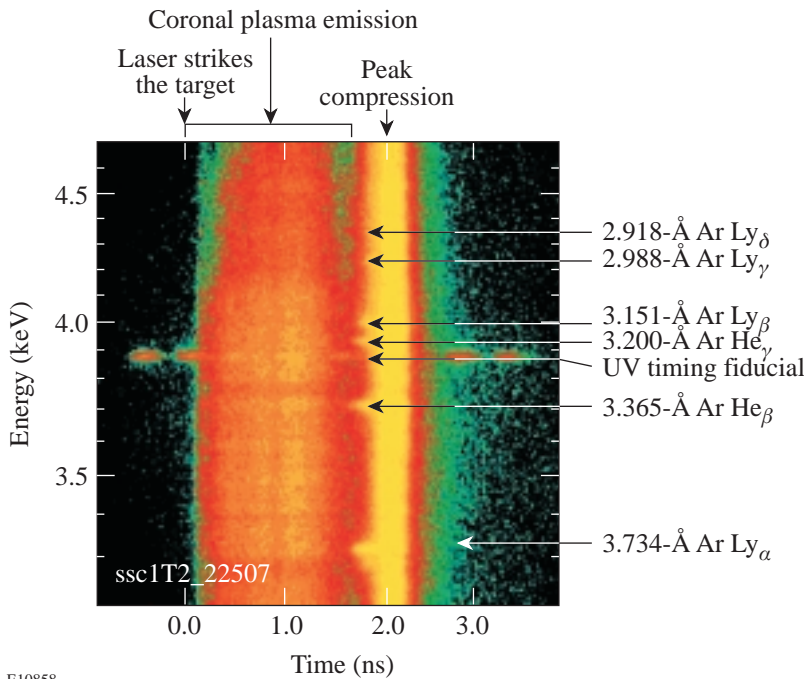


Figure 86.3
The time-resolved Ar *K*-shell spectral measurement with an ~4-ns temporal window for shot number 22507 with temporal streak distortions removed. The entire evolution of the x-ray emission from the start of the coronal plasma emission when the laser strikes the target to the peak x-ray production at peak compression is recorded. The time axis was established with the temporally modulated ultraviolet fiducial laser pulse, and the exponential rise of the coronal plasma emission was extrapolated back to the beginning of the laser pulse.

E10858

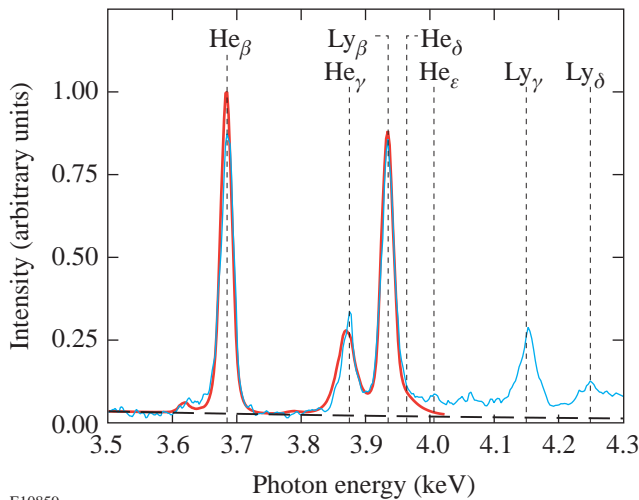


Figure 86.4
The measured spectrum (blue curve) observed just after the onset of the Ar *K*-shell emission lines at $t = 1.77$ ns is used to establish the photon-energy scale. The inferred electron density and temperature from the modeled spectrum for the 3.5- to 4.0-keV range (red curve) are $0.3 (\pm 0.03) \times 10^{24} \text{ cm}^{-3}$ and $1.3 (\pm 0.07) \text{ keV}$. The background bremsstrahlung emission spectrum is represented by the dashed curve. The vertical dotted lines represent the unshifted line centers of the Ar *K*-shell resonance lines. At present only the 3.5- to 4.0-keV range is analyzed; however, work is in progress for the spectrum above 4.0 keV, which is more challenging to model due to the presence of the He-like and H-like bound-free edges.

E10859

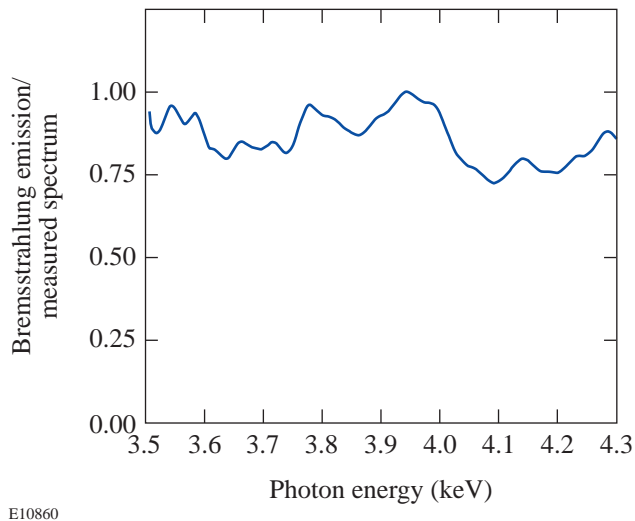


Figure 86.5

The photometric calibration of the streaked spectra to correct for variations in x-ray spectral sensitivity and streak camera flat-fielding effects is determined by recording continuum emission from an implosion with no Ar-dopant simultaneously on the time-resolved and time-integrated instruments. The measured time-integrated spectrum was modeled with a bremsstrahlung emission spectrum characteristic of an electron temperature equal to 0.68 keV. The time-resolved measurement was integrated in time and compared with the modeled spectrum. The ratio of the modeled emission to the measurement is the photometric calibration of the streaked measurement.

MERL utilizes the adjustable parameter exponential approximation (APEX)²⁸ for ion microfield calculation, the theory of Boercker, Iglesias, and Dufty (BID)²⁹ for the ion dynamics, and a quantum mechanical relaxation approximation for electron broadening.⁸

Ar *K*-shell spectra were calculated for many combinations of electron temperatures and densities. Collisional-radiative-equilibrium population distributions including 1380 levels (1 fully stripped, 25 H-like, 372 He-like, 918 Li-like, 28 Be-like, 15 B-like, 11 C-like, and 10 N-like) are solved using the CRETIN code.³⁰ The effects on the populations due to radiative transfer of the optically thick Ly_α and $\text{He}_\alpha(1s2l-1s^2)$ emissions are approximated using Mancini's escape factors.³¹ The Stark-broadened Ar *K*-shell resonance lines and satellites are calculated with MERL,²⁷ and opacity broadening is calculated assuming uniform core conditions.

The best fit to the measured spectra in the 3.5- to 4.0-keV range is determined using a least squares fitting routine. A look-up table is generated for 4000 combinations of electron temperature and densities in the range of interest. For each time-resolved measurement, the bremsstrahlung emission in

the 3.5- to 4.0-keV range is fitted in the measured spectra and added to the modeled Ar *K*-shell spectra. Modeled spectra are convolved with the spectral resolution of the streaked measurement, which was determined using the narrow spectral features that are observed when the Ar *K*-shell lines initially light up. The fitting routine searches the look-up table for the best fit for each time-resolved spectrum. At present only the 3.5- to 4.0-keV range is analyzed; however, work is in progress for the spectrum above 4.0 keV, which is more challenging to model due to the presence of the He-like and H-like bound-free edges.

Experimental Results and Analysis

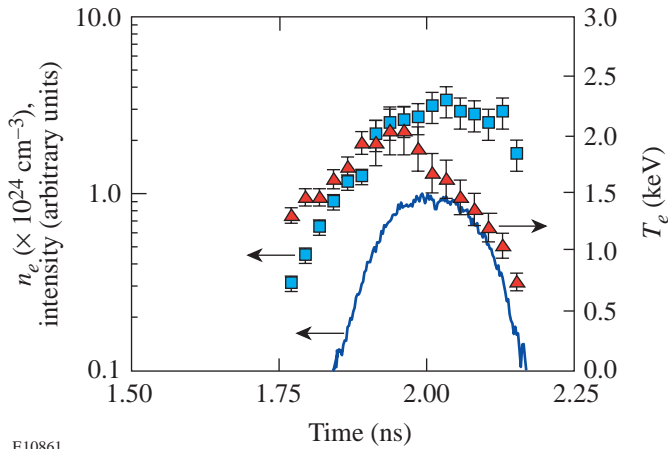
Significant changes in the Stark-broadened line widths and the relative ratios of the Ar *K*-shell emissions occur during the course of the implosion, making this diagnostic sensitive to the core electron temperature and density. A time history of emissivity-averaged core electron temperature (triangles) and density (squares) inferred from the time-resolved Ar *K*-shell spectroscopy is shown in Fig. 86.6. The measured x-ray continuum in the 3.50- to 3.55-keV range (blue line) is also shown for reference. An examination of Fig. 86.6 reveals the electron temperature peaks first, then the electron density peaks around the time of peak x-ray production. The electron temperature inferred from fitting the bremsstrahlung emission in the 3.5- to 4.0-keV spectral range slowly decreases with time from ~ 0.8 keV at $t = 1.77$ ns to ~ 0.5 keV at 2.15 ns.

As pointed out earlier in the **Experimental Setup** section, the Ar *K*-shell emission lines at early times are used to establish the photon energy scale (see Fig. 86.4). The narrow spectral features that are measured (blue curve) in the 3.5- to 4.0-keV range are modeled (red curve) with the spectral line shapes characteristic of core conditions with electron density and temperature of $0.3 (\pm 0.03) \times 10^{24} \text{ cm}^{-3}$ and 1.3 (± 0.07) keV. The error analysis of the inferred electron temperature and density is given below. The level of continuum emission is also shown in Fig. 86.4 (dashed line), and the vertical dotted lines represent the unshifted line centers of the Ar *K*-shell resonance lines. Selected spectra from the hot, dense plasma are examined below.

The spectrum recorded at 1.89 ns is shown in Fig. 86.7 along with the modeled spectrum. The inferred electron density and temperature are $1.25 (\pm 0.13) \times 10^{24} \text{ cm}^{-3}$ and 1.9 (± 0.1) keV. Line shifts to lower photon energies¹⁰ can be readily observed in the He_β , Ly_β , and Ly_γ by comparing the measured profiles with the position of the unshifted lines. The atomic physics model shows good agreement with the mea-

sured line shifts, which are observed throughout the high-density portion of the implosion. Compared with Fig. 86.4, the He_β is now weaker than the Ly_β , and the level of continuum emission has increased.

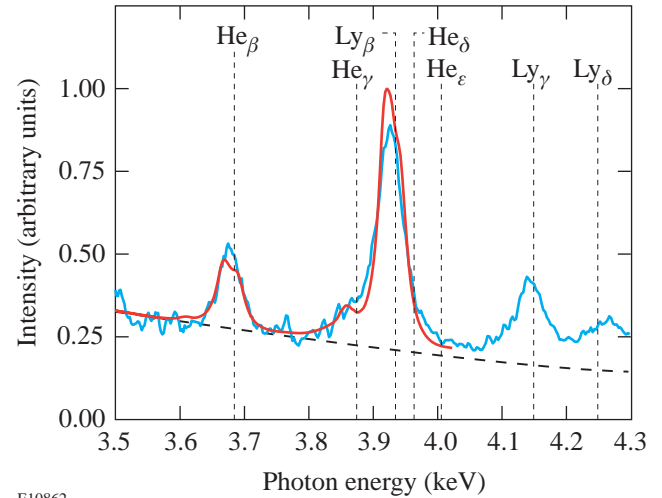
Simulations of the implosion with the 1-D hydrodynamic code *LILAC* indicate that the peak neutron production occurs at the same time as the peak emissivity-averaged electron temperature. Therefore, peak neutron production is assumed to be simultaneous with the peaking of the electron temperature at $t = 1.93$. The spectrum recorded at this time is shown in Fig. 86.8. The electron temperature and density at the time of peak neutron production are determined to be $2.0 (\pm 0.2)$ keV and $2.5 (\pm 0.5) \times 10^{24} \text{ cm}^{-3}$. This represents the highest combination of electron temperature and density measured with Ar-doped deuterium gas fill capsules in laser-driven fusion. As the implosion proceeds to peak compression, which occurs at $t = 2.01$ ns, the inferred electron density continues to increase to $3.1 (\pm 0.6) \times 10^{24} \text{ cm}^{-3}$, while the electron temperature decreases to $1.7 (\pm 0.17)$ keV. The spectrum measured at peak compression is shown in Fig. 86.9. As can be seen in Figs. 86.8 and 86.9, the background bremsstrahlung emission is comparable with the Ly_β intensity and is stronger than the He_β



E10861

Figure 86.6

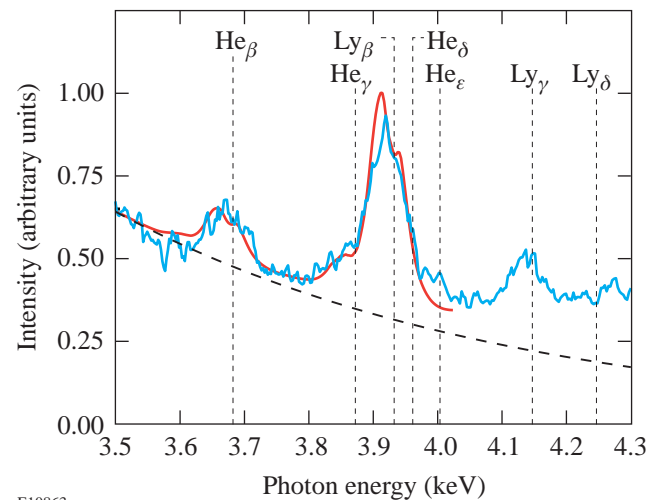
The time history of the emissivity-averaged core electron temperature (triangles) and density (squares) inferred from the time-resolved Ar *K*-shell spectroscopy for shot number 22507 reveals that the electron temperature peaks first, then the electron density peaks around the time the x-ray continuum in the 3.50- to 3.55-keV range (blue line) peaks. As the imploding shell decelerates, the emissivity-averaged electron temperature and density increase to $2.0 (\pm 0.2)$ keV and $2.5 (\pm 0.5) \times 10^{24} \text{ cm}^{-3}$ at peak neutron production ($t = 1.93$ ns), which is assumed to be simultaneous with the peaking of the electron temperature. This is followed by a further increase in the electron density to $3.1 (\pm 0.6) \times 10^{24} \text{ cm}^{-3}$ and a decrease in the electron temperature to $1.7 (\pm 0.17)$ keV at peak compression ($t = 2.01$ ns).



E10862

Figure 86.7

The measured spectrum (blue curve) observed at $t = 1.89$ ns and the modeled spectrum (red curve) in the 3.5- to 4.0-keV range are presented. The inferred electron density and temperature are $1.25 (\pm 0.13) \times 10^{24} \text{ cm}^{-3}$ and $1.9 (\pm 0.1)$ keV. The background bremsstrahlung emission spectrum is represented by the dashed curve, and the unshifted line centers of the Ar *K*-shell resonance lines are represented by the vertical dotted lines. Line shifts are observed in the He_β , Ly_β , and Ly_γ lines, and an increase in the linewidths is observed.



E10863

Figure 86.8

The measured spectrum (blue curve) observed at $t = 1.93$ ns and the modeled spectrum (red curve) in the 3.5- to 4.0-keV range are presented. The background bremsstrahlung emission spectrum is represented by the dashed curve, and the unshifted line centers of the Ar *K*-shell resonance lines are represented by vertical dotted lines. The inferred electron temperature and density are $2.0 (\pm 0.2)$ keV and $2.5 (\pm 0.5) \times 10^{24} \text{ cm}^{-3}$. The peak neutron production is estimated to occur at this time with the peaking of the electron temperature.

intensity. Finally, as the compressed core disassembles, the electron temperature and density rapidly decrease. The spectrum recorded at $t = 2.15$ ns is shown in Fig. 86.10. The inferred electron density and temperature are $1.7 (\pm 0.3) \times 10^{24} \text{ cm}^{-3}$ and $0.75 (\pm 0.08)$ keV. The dominant feature of the spectrum is the He_β and its Li-like satellites around 3.55 to 3.75 keV.

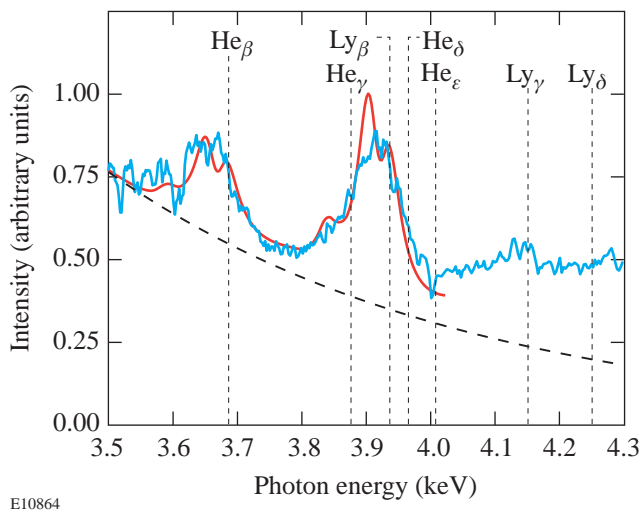
Many factors affect the accuracy of the electron temperature and density measurements. In this experiment strong signals of the spectral lines of interest were recorded throughout the implosion; therefore, the most influential factors affecting the accuracy are the determination of the background bremsstrahlung emission spectrum and the accuracy of the atomic physics model. As shown in the time-resolved spectra, the Stark-broadened spectral lines have a significant continuum emission background, which must be accounted for in the spectral line fitting procedure. Although the spectral fits examined here show good agreement with the measured line shapes and with the background levels between the spectral lines, there is some discrepancy between the measured and modeled line shapes at the peaks of the lines. The accuracy in the electron density is estimated to be $\pm 10\%$, and the accuracy in the electron temperature is estimated to be $\pm 5\%$ for the range of electron densities below $2 \times 10^{24} \text{ cm}^{-3}$. Above this density

the accuracy in the electron density is estimated to be $\pm 20\%$, and the accuracy in the electron temperature is estimated to be $\pm 10\%$. The precision of the least squares spectral line fitting routine is well within the accuracy error.

Work is in progress to compare time-resolved Ar K -shell spectroscopy measurements with the time-resolved neutron burn history to establish the timing between the peak neutron burn and peak x-ray production. Comparisons will be made between fuel- ρR measurements, gated x-ray images of the core, and the emissivity-averaged core electron density measurement to estimate the amount of mix in the core of shell material with the fuel. In addition, lower dopant levels of Ar were studied to minimize the impact of the enhanced radiative losses on the target performance, while maintaining detectable signals of the Ar K -shell emission. These results will be presented in a separate publication for a range of targets with predicted convergence ratios from 13 to 37.

Conclusion

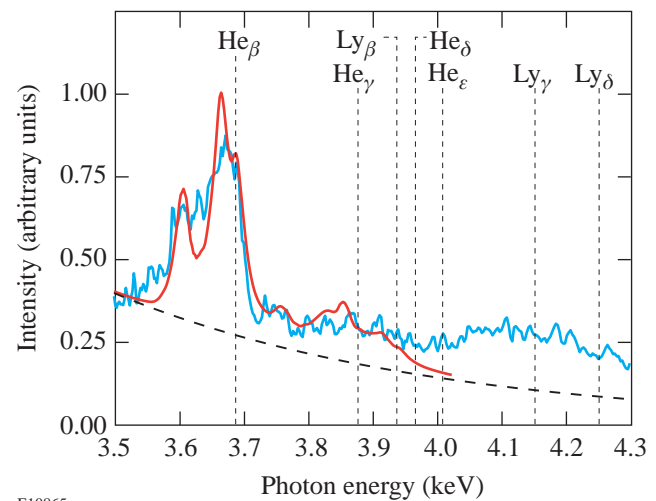
Time-resolved Ar K -shell spectroscopy has been used to diagnose the core conditions of direct-drive implosions on the 60-beam OMEGA laser system. Plastic shells with an Ar-doped deuterium fill gas were driven with a 23-kJ, 1-ns square laser pulse with a predicted convergence ratio of ~ 15 , and laser



E10864

Figure 86.9

The measured spectrum (blue curve) observed at $t = 2.01$ ns and the modeled spectrum (red curve) in the 3.5- to 4.0-keV range are presented. The background bremsstrahlung emission spectrum is represented by the dashed curve, and the unshifted line centers of the Ar K -shell resonance lines are represented by the vertical dotted lines. Peak compression occurs at this time, and the inferred electron temperature and density are $1.7 (\pm 0.17)$ keV and $3.1 (\pm 0.6) \times 10^{24} \text{ cm}^{-3}$.



E10865

Figure 86.10

The measured spectrum (blue curve) observed at $t = 2.15$ ns and the modeled spectrum (red curve) in the 3.5- to 4.0-keV range are presented. The background bremsstrahlung emission spectrum is represented by the dashed curve, and the unshifted line centers of the Ar K -shell resonance lines are represented by the vertical dotted lines. The compressed core is disassembling, and the inferred electron temperature and density rapidly decrease to $0.75 (\pm 0.08)$ keV and $1.7 (\pm 0.3) \times 10^{24} \text{ cm}^{-3}$.

beams were smoothed with 1-THz SSD and polarization smoothing using birefringent wedges. The measured time-dependent, Stark-broadened, Ar *K*-shell spectral line shapes were compared with modeled spectra to infer the emissivity-averaged core electron temperature and density. As the imploding shell decelerates, the emissivity-averaged electron temperature and density increase to 2.0 (± 0.2) keV and 2.5 (± 0.5) $\times 10^{24}$ cm $^{-3}$ at peak neutron production, which is assumed to occur at the time of the peak emissivity-averaged electron temperature. This is followed by a further increase in the electron density to 3.1 (± 0.6) $\times 10^{24}$ cm $^{-3}$ and a decrease in the electron temperature to 1.7 (± 0.17) keV at peak compression.

ACKNOWLEDGMENT

This work was supported by the U. S. Department of Energy Office of Inertial Confinement Fusion under Cooperative Agreement No. DE-FC03-92SF19460, the University of Rochester, and the New York State Energy Research and Development Authority. The support of DOE does not constitute an endorsement by DOE of the views expressed in this article.

REFERENCES

1. C. P. Verdon, *Bull. Am. Phys. Soc.* **38**, 2010 (1993).
2. S. E. Bodner, D. G. Colombant, J. H. Gardner, R. H. Lehmburg, S. P. Obenschain, L. Phillips, A. J. Schmitt, J. D. Sethian, R. L. McCrory, W. Seka, C. P. Verdon, J. P. Knauer, B. B. Afeyan, and H. T. Powell, *Phys. Plasmas* **5**, 1901 (1998).
3. B. Yaakobi, S. Skupsky, R. L. McCrory, C. F. Hooper, H. Deckman, P. Bourke, and J. M. Soures, *Phys. Rev. Lett.* **44**, 1072 (1980).
4. A. Hauer *et al.*, *Phys. Rev. A* **28**, 963 (1983).
5. C. F. Hooper, Jr., D. P. Kilcrease, R. C. Mancini, L. A. Woltz, D. K. Bradley, P. A. Jaanimagi, and M. C. Richardson, *Phys. Rev. Lett.* **63**, 267 (1989).
6. H. R. Griem, *Phys. Fluids B* **4**, 2346 (1992).
7. C. F. Hooper, Jr., R. C. Mancini, D. A. Haynes, Jr., and D. T. Garber, in *Elementary Processes in Dense Plasmas*, edited by S. Ichimaru and S. Ogata (Addison-Wesley, Reading, MA, 1995), pp. 403–414.
8. D. A. Haynes, Jr., D. T. Garber, C. F. Hooper, Jr., R. C. Mancini, Y. T. Lee, D. K. Bradley, J. Delettrez, R. Epstein, and P. A. Jaanimagi, *Phys. Rev. E* **53**, 1042 (1996).
9. D. K. Bradley, J. A. Delettrez, R. Epstein, R. P. J. Town, C. P. Verdon, B. Yaakobi, S. Regan, F. J. Marshall, T. R. Boehly, J. P. Knauer, D. D. Meyerhofer, V. A. Smalyuk, W. Seka, D. A. Haynes, Jr., M. Gunderson, G. Junkel, C. F. Hooper, Jr., P. M. Bell, T. J. Ognibene, and R. A. Lerche, *Phys. Plasmas* **5**, 1870 (1998).
10. G. C. Junkel *et al.*, *Phys. Rev. E* **62**, 5584 (2000).
11. B. A. Hammel *et al.*, *Phys. Rev. Lett.* **70**, 1263 (1993).
12. C. J. Keane *et al.*, *Phys. Fluids B* **5**, 3328 (1993).
13. B. A. Hammel *et al.*, *J. Quant. Spectrosc. Radiat. Transf.* **51**, 113 (1994).
14. H. Nishimura *et al.*, *Phys. Plasmas* **2**, 2063 (1995).
15. N. C. Woolsey *et al.*, *Phys. Rev. E* **56**, 2314 (1997).
16. N. C. Woolsey *et al.*, *Phys. Rev. E* **57**, 4650 (1998).
17. T. R. Boehly, D. L. Brown, R. S. Craxton, R. L. Keck, J. P. Knauer, J. H. Kelly, T. J. Kessler, S. A. Kumpan, S. J. Loucks, S. A. Letzring, F. J. Marshall, R. L. McCrory, S. F. B. Morse, W. Seka, J. M. Soures, and C. P. Verdon, *Opt. Commun.* **133**, 495 (1997).
18. T. J. Kessler, Y. Lin, J. J. Armstrong, and B. Velazquez, in *Laser Coherence Control: Technology and Applications*, edited by H. T. Powell and T. J. Kessler (SPIE, Bellingham, WA, 1993), Vol. 1870, pp. 95–104; Y. Lin, T. J. Kessler, and G. N. Lawrence, *Opt. Lett.* **21**, 1703 (1996).
19. S. Skupsky, R. W. Short, T. Kessler, R. S. Craxton, S. Letzring, and J. M. Soures, *J. Appl. Phys.* **66**, 3456 (1989).
20. S. Skupsky and R. S. Craxton, *Phys. Plasmas* **6**, 2157 (1999).
21. S. P. Regan, J. A. Marozas, J. H. Kelly, T. R. Boehly, W. R. Donaldson, P. A. Jaanimagi, R. L. Keck, T. J. Kessler, D. D. Meyerhofer, W. Seka, S. Skupsky, and V. A. Smalyuk, *J. Opt. Soc. Am. B* **17**, 1483 (2000).
22. T. R. Boehly, V. A. Smalyuk, D. D. Meyerhofer, J. P. Knauer, D. K. Bradley, R. S. Craxton, M. J. Guardalben, S. Skupsky, and T. J. Kessler, *J. Appl. Phys.* **85**, 3444 (1999).
23. T. R. Boehly, V. N. Goncharov, O. Gotchev, J. P. Knauer, D. D. Meyerhofer, D. Oron, S. P. Regan, Y. Srebro, W. Seka, D. Shvarts, S. Skupsky, and V. A. Smalyuk, *Phys. Plasmas* **8**, 2331 (2001).
24. D. D. Meyerhofer, J. A. Delettrez, R. Epstein, V. Yu. Glebov, V. N. Goncharov, R. L. Keck, R. L. McCrory, P. W. McKenty, F. J. Marshall, P. B. Radha, S. P. Regan, S. Roberts, W. Seka, S. Skupsky, V. A. Smalyuk, C. Sorce, C. Stoeckl, J. M. Soures, R. P. J. Town, B. Yaakobi, J. D. Zuegel, J. Frenje, C. K. Li, R. D. Petraso, D. G. Hicks, F. H. Séguin, K. Fletcher, S. Padalino, M. R. Freeman, N. Izumi, R. Lerche, T. W. Phillips, and T. C. Sangster, *Phys. Plasmas* **8**, 2251 (2001).
25. D. H. Kalantar *et al.*, in *22nd International Congress on High-Speed Photography and Photonics*, edited by D. L. Paisley and A. M. Frank (SPIE, Bellingham, WA, 1997), Vol. 2869, pp. 680–685.
26. B. L. Henke, E. M. Gullikson, and J. C. Davis, *At. Data Nucl. Data Tables* **54**, 181 (1993).
27. R. C. Mancini *et al.*, *Comput. Phys. Commun.* **63**, 314 (1991).
28. C. A. Iglesias, J. L. Lebowitz, and D. MacGowan, *Phys. Rev. A* **28**, 1667 (1983).
29. D. B. Boercker, C. A. Iglesias, and J. W. Dufty, *Phys. Rev. A* **36**, 2254 (1987).
30. H. A. Scott and R. W. Mayle, *Appl. Phys. B* **B58**, 35 (1994).
31. R. C. Mancini, R. F. Joyce, and C. F. Hooper, Jr., *J. Phys. B: At. Mol. Phys.* **20**, 2975 (1987).